



HAL
open science

Passive Mode-Locking and Tilted Waves in Broad-Area Vertical-Cavity Surface-Emitting Lasers

Mathias Marconi, Julien Javaloyes, Salvador Balle, Massimo Giudici

► **To cite this version:**

Mathias Marconi, Julien Javaloyes, Salvador Balle, Massimo Giudici. Passive Mode-Locking and Tilted Waves in Broad-Area Vertical-Cavity Surface-Emitting Lasers. 2014. hal-00943530v4

HAL Id: hal-00943530

<https://hal.science/hal-00943530v4>

Preprint submitted on 26 Jun 2014

HAL is a multi-disciplinary open access archive for the deposit and dissemination of scientific research documents, whether they are published or not. The documents may come from teaching and research institutions in France or abroad, or from public or private research centers.

L'archive ouverte pluridisciplinaire **HAL**, est destinée au dépôt et à la diffusion de documents scientifiques de niveau recherche, publiés ou non, émanant des établissements d'enseignement et de recherche français ou étrangers, des laboratoires publics ou privés.

Passive Mode-Locking and Tilted Waves in Broad-Area Vertical-Cavity Surface-Emitting Lasers

M. Marconi, J. Javaloyes, *Member, IEEE*, S. Balle, *Member, IEEE*, and M. Giudici *Member, IEEE*.

Abstract—We show experimentally and theoretically that an electrically biased 200 μm multi-transverse mode Vertical-Cavity Surface-Emitting Laser can be passively mode-locked using optical feedback from a distant Resonant Saturable Absorber Mirror. This is achieved when one cavity is placed at the Fourier plane of the other. Such non conventional optical feedback leads to the formation of two tilted plane waves traveling in the external cavity with opposite transverse components and alternating in time at every round-trip. Each of these plane waves gives birth to a train of mode-locked pulses separated by twice the external cavity round-trip, while the two trains are time shifted by a round-trip. A large portion of the transverse section of the device contributes to mode-locked emission leading to pulses of approximately 1 W peak power and 10 ps width. We discuss how inhomogeneities in the transverse section of the saturable absorber select the emitted tilted waves, thus leading to tunable emission over 4 nm.

Index Terms—Mode-Locking, Broad-Area Lasers, VCSELs

I. INTRODUCTION

LASER mode-locking (ML) is a fascinating self-organized cooperative effect involving a large number of longitudinal modes that was recently linked to out-of-equilibrium phase transitions [1]. From a practical point of view many applications require sources of short pulses like e.g. medicine, metrology and communications [2]. Passive ML (PML) is arguably one of the most elegant method to obtain such pulses. It is achieved by combining two elements, a laser amplifier providing gain and a saturable absorber acting as a pulse shortening element. Under appropriate conditions, the different dynamical properties of the absorption and of the gain favor pulsed emission by creating a limited time window for amplification around an intensity pulse [3], [4]. PML can also be achieved using artificial absorbers like e.g. nonlinear polarization rotation [5], Kerr lens mode-locking [6], Crossed-Polarization [7] or Stark effect modulation [8]. The PML mechanism has led to the shortest and most intense optical pulses ever generated and pulses in the femto-second range are produced by dye [9] and solid-state lasers [10]. However, the large size of these devices and the need for optical pumping strongly limit their application domain.

M. Marconi and M. Giudici are with the Institut Non Linéaire de Nice, Université de Nice Sophia Antipolis - Centre National de la Recherche Scientifique, 1361 route des lucioles, F-06560 Valbonne, France, e-mails: mathias.marconi@inln.cnrs.fr and massimo.giudici@inln.cnrs.fr.

J. Javaloyes is with the Departament de Física, Universitat de les Illes Balears, C/ Valldemossa, km 7.5, E-07122 Palma de Mallorca, Spain, e-mail: julien.javaloyes@uib.es

S. Balle is with the Institut Mediterrani d'Estudis Avançats, CSIC-UIB, E-07071 Palma de Mallorca, Spain, e-mail: salvador@imedea.uib-csic.es

More compact solutions can be envisaged using semiconductor devices: PML is obtained in monolithic edge-emitting semiconductor lasers which have the advantage of being electrically biased and to operate at high repetition rates (1 ~ 160 GHz) although the peak powers that can be obtained are usually limited because of Catastrophic Optical Damage (COD) [11]. Large output peak power in the kilowatt range is commonly achieved by coupling Vertical-External-Cavity Surface-Emitting Lasers (VECSEL) with a Semiconductor Saturable Absorber Mirror [12], [13]. The external cavity is designed to operate in the fundamental Gaussian mode while a large section of the VECSEL is optically pumped to achieve large power, in this configuration the external cavity length leads to repetition rates from a few to tens of GHz. In both monolithic and external-cavity schemes, the presence of higher order transverse modes of the resonator is usually perceived as detrimental for mode-locking stability and it is avoided by cavity design. In fact, when several higher order modes are present, the emission profile is usually not stationary [14], and even chaotic filamentation may occur [15]. This is due to thermal effects imposing a current-dependent refractive index profile, and to the so-called Spatial Hole Burning (SHB). This phenomenon occurs in regions of high optical intensity, where the local gain (and thus the local carrier density) is depressed by stimulated emission, hence leading to a local increase of refractive index which contributes to strengthen light confinement and to further increase the local field intensity. On the other hand, the possibility of achieving a cooperative effect of transverse modes where they would contribute coherently to longitudinal mode locking is very attractive for increasing the pulse power, since it would allow to circumvent COD.

In this work we propose a scheme for achieving mode-locking using an electrically biased, 200 μm section Vertical-Cavity Surface-Emitting Laser (VCSEL). This device is mounted in an external cavity configuration closed by a Resonant Saturable Absorber Mirror (RSAM). Mode-locking is obtained when placing the RSAM in the exact Fourier transform plane of the VCSEL near-field profile, i.e. when imaging the VCSEL far-field profile onto the RSAM. As a consequence, the VCSEL profile is imaged onto itself after a single external cavity round-trip, but inverted. This corresponds to a transverse magnification of -1. We show that such configuration leads to the generation of two tilted plane waves traveling in the external cavity with an opposite transverse component and alternating each other at every round-trip. Each one of these plane waves gives birth to a train of mode-locked pulses separated by twice the external cavity round trip ($2\tau_e$), while the two trains are time shifted of τ_e . Almost the entire

89 transverse section of the VCSEL contributes to mode-locking
 90 leading to pulses of 10 ps width and peak power around
 91 1 W. We analyze the mechanism leading to the selection of
 92 the tilted waves and we demonstrate a technique for tuning
 93 the central wavelength of the mode-locked emission. Our
 94 experimental findings are confirmed by a spatially resolved
 95 model for the VCSEL and the RSAM taking into account
 96 the multiple reflections in the external cavity and our specific
 97 imaging conditions.

98 II. EXPERIMENT

99 The VCSEL is a 980 nm device manufactured by ULM
 100 Photonics [16]. Its standalone threshold current (J_{st}) is about
 101 380 mA, though emission is localized only at the external
 102 perimeter of the device up to $J = 850$ mA, after which roll-
 103 off starts to occur. The 980 nm RSAM (BaTop GmbH) has
 104 a transverse dimension of 4×4 mm² and it exhibits a low
 105 unsaturated reflectivity of 1% that increases up to 60% when
 106 saturated. The RSAM saturation fluence is $15 \mu\text{J}\cdot\text{cm}^{-2}$. These
 107 values are obtained at the RSAM resonant wavelength which
 108 can be thermally tuned over 3 nm (between $T_1 = 10^\circ\text{C}$ and
 109 $T_2 = 50^\circ\text{C}$). The Full Width at Half Maximum (FWHM)
 110 of the RSAM resonance is around 16 nm and the saturable
 111 absorption recovery time is around 1 ps.

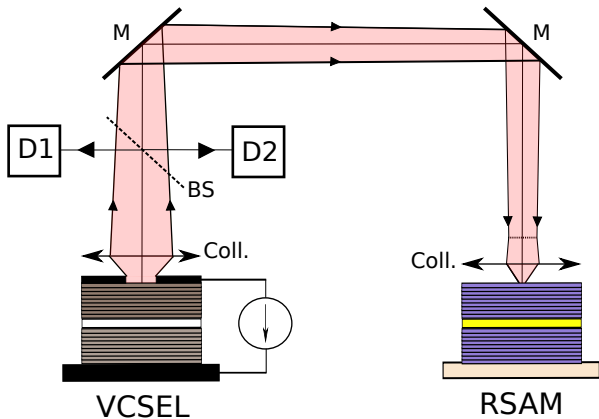


Figure 1. Experimental Set-up: Temperature-stabilized VCSEL and RSAM. Coll.: Aspheric Lens, BS : Beam Splitter, M: Mirror and D1/D2: Detectors and CCD cameras.

112 The set up is shown in Fig. 1. Both the VCSEL and RSAM
 113 are mounted on temperature controlled substrates which allow
 114 for tuning the resonance frequency of each cavity; parameters
 115 are set for having the emission of the VCSEL resonant with
 116 the RSAM. The light emitted by the VCSEL is collected by
 117 a large numerical aperture (0.68) aspheric lens and a similar
 118 lens is placed in front of the RSAM. A 10% reflection beam
 119 splitter allows for light extraction from the external cavity and
 120 to monitor both the VCSEL and the RSAM outputs. Intensity
 121 output is monitored by a 33 GHz oscilloscope coupled with
 122 fast 10 GHz detector. Part of the light is sent to two CCD cam-
 123 eras; the first one records the near-field profile of the VCSEL,
 124 while the second records the VCSEL's far-field profile. The
 125 light reflected by the RSAM is also used for monitoring and a
 126 third CCD camera records the light on the RSAM surface. The
 127 external cavity length is fixed to $L = 30$ cm. One of the most

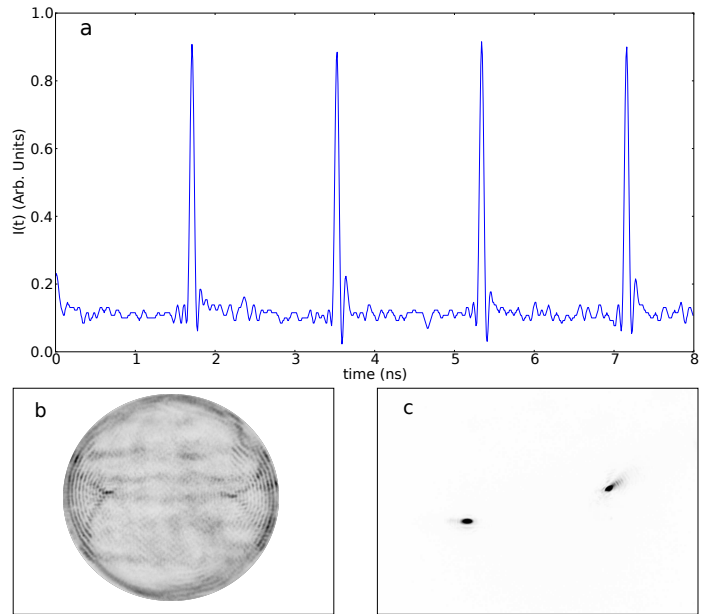


Figure 2. Panel a): Temporal trace of the VCSEL in the mode-locked regime. Panel b): Corresponding Near-Field emission of VCSEL. Panel c): Corresponding Far-field emission from the VCSEL. Intensity grows from white to black. $J=600$ mA.

128 important parameters for achieving mode-locking in this setup
 129 is the imaging condition of the VCSEL onto the RSAM. We
 130 obtain mode-locking when the RSAM is placed in the plane
 131 where the exact Fourier transform of the VCSEL near-field
 132 occurs. This working condition is obtained by imaging the
 133 VCSEL near-field profile onto the front focal plane of the
 134 aspheric lens placed in front of the RSAM, while the RSAM
 135 is placed onto the back focal plane of this lens. We remark
 136 that this leads to a non-local feedback from the RSAM onto
 137 the VCSEL: if the RSAM were a normal mirror, the VCSEL
 138 near-field profile would be inversely imaged onto itself after
 139 a cavity round-trip.

140 Panel a) in Fig. 2 displays the time trace of the VCSEL
 141 in the mode-locking regime which consists of a regular train
 142 of pulses with a period equal to the round-trip time in the
 143 external cavity $\tau_e = 2L/c = 2$ ns. The pulse width cannot be
 144 determined from the oscilloscope traces, which are limited by
 145 our real-time detection system (10 GHz effective bandwidth).
 146 However, an estimate of the pulse width can be obtained
 147 from the optical spectrum of the output, which exhibits a
 148 broad spectral peak whose FWHM is around 0.12 nm that
 149 corresponds, assuming a time-bandwidth product of 0.4, to a
 150 pulse width of 10 ps FWHM. The pulse was also detected by
 151 a 42 GHz detector, which confirms a pulse width of less than
 152 12 ps FWHM considering the oscilloscope bandwidth limit.

153 Panels b) and c) in Fig. 2 show the time-averaged near-
 154 field and far-field profiles of the VCSEL, respectively. In
 155 addition, we verified that the image of the RSAM surface
 156 (not shown) is very similar to Fig. 2c), thus revealing that
 157 the RSAM is effectively placed in the Fourier plane of the
 158 VCSEL's near-field. The far-field of the VCSEL exhibits two
 159 bright, off-axis spots that indicate the presence of two counter-
 160 propagating tilted waves along the cross section of the VCSEL.

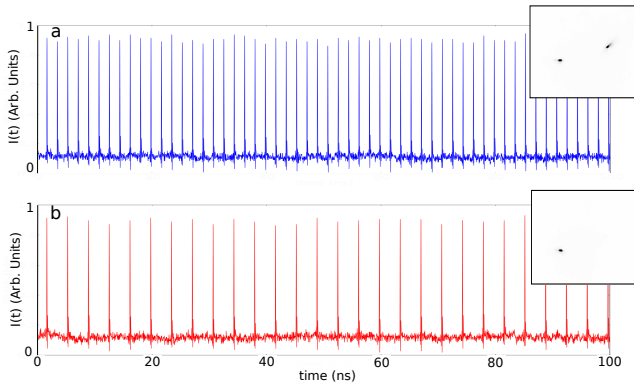


Figure 3. Temporal signal obtained when detecting simultaneously the two spots (panel a) of the far-field emission of the VCSEL or a single spot (panel b). The insets represent the detected spots in the far-field.

161 The transverse wave vector of each of these waves is related in
 162 direction and modulus to the position of the spots, and their
 163 symmetry with respect to the optical axis indicates that the
 164 two transverse wave vectors are one opposite to the other.

165 Remarkably, however, no interference pattern is visible in
 166 the near-field emission of the VCSEL. The concentric rings
 167 close to the limit of the VCSEL arise from current crowding
 168 [17] and do not contribute significantly to the bright spots
 169 in the far-field, as it was verified by filtering them out. The
 170 lack of interference pattern between the counter-propagating
 171 waves in the time-averaged near field implies that these waves
 172 are not simultaneously present; they rather should alternate
 173 each other in time. This is apparent in Fig. 3, where the time
 174 trace obtained from the whole far-field is compared to the one
 175 obtained by detecting only one of the two bright spots. While
 176 the former trace has the characteristics discussed above, the
 177 latter trace consists of a periodic train of pulses at a period
 178 $2\tau_e$. Thus the trace from the whole far-field is obtained by
 179 interleaving two identical pulse trains of period $2\tau_e$ with a time
 180 delay τ_e one with respect to the other, each train corresponding
 181 to a tilted wave with opposite transverse wave vector.

182 This mode-locked dynamics does not depend critically on
 183 the transverse wave vector value selected by the system. Such
 184 value can be modified by shifting the RSAM device laterally
 185 (i.e. along the back focal plane of its collimating lens) or
 186 slightly displacing the collimating lens off the axis defined
 187 by the centers of the VCSEL and the RSAM. The change in
 188 selected transverse wave vector is evidenced by the variations
 189 in the separation between the two spots on the RSAM mirror,
 190 as shown in Fig. 4. The position of each spot on the RSAM
 191 with respect to the optical axis is related to the transverse wave
 192 vector $\vec{K}_\perp = \vec{K} - \vec{K}_0$ of the plane wave by

$$\vec{r}_s = \lambda f \frac{\vec{K}_\perp}{2\pi},$$

193 where f is the focal length of the lens in front of the RSAM,
 194 λ is the wavelength of the light, \vec{K} is the wave vector emitted
 195 by the VCSEL while \vec{K}_0 is its component along the cavity
 196 axis. Although substantial changes in emission wavelength
 197 —over 4 nm tuning— can be induced in this way, it is
 198 observed that within a wide parameter range, the temporal

199 characteristics of the pulse train do not change. This fact opens
 200 very interesting possibilities in terms of wavelength tuning
 201 and of beam stirring of a mode-locked emission. The only
 202 noticeable effect of varying the position of the spot is a slight
 203 reduction of the pulse peak power. We attribute this effect
 204 to the increased losses experienced in the external cavity by
 205 wave vectors with large K_\perp as a result of the DBRs reflectivity
 206 angular dependence and/or the finite numerical aperture of the
 207 collimating lenses. This point will be further discussed in the
 208 theoretical section.

209 Beyond the maximal separation of the two spots on the
 210 RSAM shown in Fig. 4, mode-locking is suddenly lost.
 211 Importantly, mode-locking strongly deteriorates in regularity
 212 when the two spots are brought to coincide, leading, in some
 213 cases, to CW emission. Hence, in our setup, regular mode-
 214 locking was not achieved with $K_\perp \simeq 0$, i.e. for a plane-wave
 215 emission almost parallel to the optical axis of the VCSEL.

216 The mode-locking regime is stable in a very broad range
 217 of the VCSEL current, namely $285 \text{ mA} < J < 703 \text{ mA}$. If
 218 the bias current is varied within this range while keeping the
 219 alignment, the separation of the two bright spots in the far-field
 220 profile remains constant, see Fig. 5. However the spectral peak
 221 corresponding to the mode-locking emission redshifts from
 222 976 nm ($J = 285 \text{ mA}$) up to 978 nm ($J = 703 \text{ mA}$) due to
 223 Joule heating of the VCSEL. Therefore, the selection of K_\perp
 224 does not depend on the detuning between the two cavities, at
 225 least in the range spanned.

226 We also found that, for the external cavity length considered,
 227 the PML regime is bistable with the off solution for $J < J_{st}$,
 228 see [18] for details. In these conditions and after setting the
 229 system in the off solution, we were able to start PML emission
 230 by perturbing optically the RSAM section at the point where
 231 one of the two spots appears when the system operates in
 232 the PML regime. The local perturbation has been realized by
 233 injecting an external coherent beam tuned with the RSAM
 234 cavity resonance and having a waist diameter of less than
 235 $10 \mu\text{m}$.

III. DISCUSSION OF THE EXPERIMENTAL EVIDENCES

237 These observations disclose a possible explanation about the
 238 emergence of the mode-locking regime in our system. From
 239 the dynamical point of view, mode-locking is favored when the
 240 saturable absorber is more easily saturated than the amplifier
 241 [2]. In our scheme, this is achieved when the VCSEL emits a
 242 tilted plane wave, which imposes a low power density (hence
 243 low saturation) in the gain section and, at the same time, a
 244 strong local saturation of the RSAM. The reason is that the
 245 VCSEL and the RSAM lie one into the Fourier plane of the
 246 other and in these conditions any plane wave emitted by the
 247 VCSEL yields a spot on the RSAM and vice-versa. On the
 248 other hand, the unsaturated reflectivity of the RSAM is very
 249 low ($\sim 1\%$) at resonance, rising up to $\sim 60\%$ when fully
 250 saturated. Hence, if the VCSEL emits a pulse in the form of a
 251 plane wave with a transverse wave vector \vec{K}_\perp , all the power
 252 will concentrate on a single spot at \vec{r}_s on the RSAM, hereby
 253 strongly saturating the RSAM which becomes reflective. The
 254 light thus comes back to the VCSEL, where it arrives with a

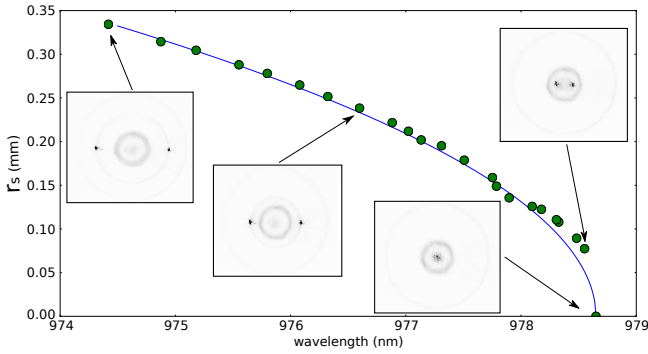


Figure 4. Off-axis position of a single spot in the far-field profile as a function of the spectral emission peak of the VCSEL. Far-field profile is shown for a discrete number of points in the graph. VCSEL emission is in the mode-locking regime for all green points of the graph while the one at the highest wavelength, where a single on-axis spot appears in the far-field profile, corresponds to an irregular dynamics. VCSEL is biased at 700 mA. The transverse wave vector is selected by laterally shifting the RSAM along the back focal plane of its collimating lens. The large size of the RSAM section (4×4 mm) with respect to the far-field size (0.7 mm at most) renders this operation feasible. The blue line has been obtained plotting $r_s = \frac{\lambda_0 f}{2\pi} \sqrt{\lambda^{-2} - \lambda_0^{-2}}$, with $\lambda_0 = 978.65$ nm and $f = 8$ mm. A similar tuning curve is obtained by laterally shifting the collimating lens of the RSAM.

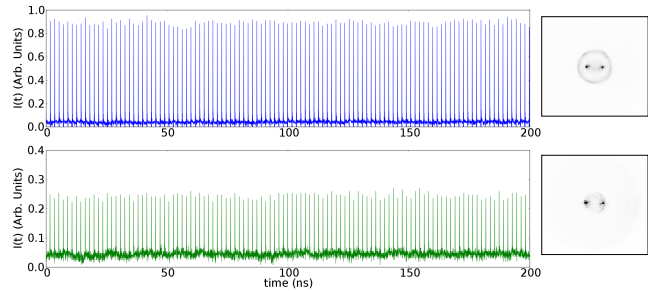


Figure 5. VCSEL time traces emission and corresponding far-field emission profile in the mode-locking regime for two values of the VCSEL bias. The upper and the lower panels correspond to $J = 703$ mA and $J = 285$ mA.

transverse component $-\vec{K}_\perp$. Upon amplification and reflection at the VCSEL, the process repeats for this plane wave with opposite transverse wave vector, which is now imaged onto the RSAM at $-\vec{r}_s$. Thus, after two round-trips the original wave at \vec{K}_\perp overlaps with itself, leading to a pulse train at twice the round-trip time for this wave which is alternating in time with a delay of one round-trip with its replica at $-\vec{K}_\perp$. This explains the observed dynamics, and also the lack of interference pattern in the form of rolls in the VCSEL near-field: even if two tilted waves are propagating within the VCSEL resonator, they alternate in time with a delay of one round-trip in the external cavity, so that they never coexist and do not yield the expected interference pattern. The two spots appearing simultaneously in the far-field (i.e. over the RSAM) are only an artifact of the time-averaging operated by the CCD camera. At variance with tilted waves leading to narrow spots onto the RSAM, the flower mode present on the external frontier of the VCSEL does not contribute to PML. In fact, the Fourier Transform of such flower mode is a radial Bessel function of large order $\sim J_m(r)$ with $m \gg 1$, which corresponds to an extended ring profile. In this case, the power

density on the RSAM remains always below the saturation fluence of the RSAM.

While the above scenario is valid for a large interval of values of the transverse wave vector \vec{K}_\perp , experimental results show that the system selects a well-defined value when operating in the PML regime. In principle, this selection may arise from several factors. On the one hand, both the VCSEL and the RSAM are Fabry-Perot cavities defined by Bragg mirrors which complex reflectivity have an angular dependence. Moreover, the reflectivity of a Fabry-Perot cavity depends not only on the wavelength but also on the angle of incidence of the light, and the resonant wavelength of the cavity blue-shifts as the incidence angle increases. This effect can be further enhanced in our system due to the compound-cavity effect. Nevertheless, experimental evidences shown in Fig. 5, where the VCSEL cavity resonance is varied over 2 nm while leaving the transverse wave vector unchanged, seems to indicate that cavities detuning do not play an important role in selecting the value of \vec{K}_\perp . This can be understood when considering that the FWHM bandwidth of the RSAM absorption curve (16 nm) is much larger than the VCSEL one (1 nm).

On the other hand, wave vector selectivity may also arise from any imperfections on the RSAM/VCSEL mirrors that break the spatial invariance. State-of-the-art fabrication process does not fully prevent from formation of small size (a few μm) defects in the transverse plane of semiconductor micro-resonators. These are in general local spatial variations of the semiconductor resonator characteristics [19], which in the case of RSAM would be mainly related to a local variation of unsaturated reflectivity. Visual inspection of the reflection profile of a transversally homogeneous injected monochromatic field onto several used RSAMs has indeed shown the existence of these local variations. Such inhomogeneities on the RSAM surface may correspond to locations where the RSAM exhibits a lower unsaturated reflectivity, hence leading the system to select the tilted wave which image on the RSAM surface coincide with one of these defect. By laterally shifting the RSAM along the back focal plane of its collimating lens, the position of the defect changes in the far-field plane, thus selecting a tilted wave with another transverse wave vector component. This leads to a continuous scan of the distance between the two spots in the far-field, as shown in Fig. 4 and a corresponding change of the emission wavelength, as expected for tilted waves. The experimental evidence of Fig. 4 seems to indicate that, in our system, the presence of these inhomogeneities is ruling the selection of the transverse wave vector. The role of small imperfections in the RSAM structure in the transverse wave vector selection is confirmed by the theoretical results in the next section.

IV. THEORETICAL RESULTS

Our model for the dynamical evolution of the fields E_j and the normalized carrier density N_j in the quantum well (QW) regions of the VCSEL ($j = 1$) and the RSAM ($j = 2$) is

deduced in detail in the appendix, and it reads

$$\dot{E}_1 = [(1 - i\alpha_1)N_1 - 1 + i\Delta_\perp + c_1\Delta_\perp^2]E_1 + h_1Y_1, \quad (1)$$

$$\dot{E}_2 = [(1 - i\alpha_2)N_2 - z + ib\Delta_\perp + c_2\Delta_\perp^2]E_2 + h_2Y_2, \quad (2)$$

$$\dot{N}_1 = \gamma_1 [J_1 - (1 + |E_1|^2)N_1] + \mathcal{D}_1\Delta_\perp N_1, \quad (3)$$

$$\dot{N}_2 = \gamma_2 [J_2 - (1 + s|E_2|^2)N_2] + \mathcal{D}_2\Delta_\perp N_2, \quad (4)$$

where $\Delta_\perp = \partial_x^2 + \partial_y^2$ is the transverse Laplacian and Y_j denotes the field injected in device j . In Eqs. (1-4) time and space are normalized to the photon lifetime κ_1^{-1} and the diffraction length in the VCSEL L_d , respectively. The complex parameter z is decomposed as $z = a - i\delta$ where a represents the ratio of the photon decay rates between the VCSEL and the RSAM cavities and δ is the scaled detuning between the two cavity resonances. The scaled carrier recovery rates and the biases are denoted γ_j and J_j respectively. We define the ratio of the saturation intensities of the VCSEL and the RSAM as s . The angular dependence from the reflectivity of the DBR mirrors as well as the one stemming from the Fabry-Perot cavities are contained in the transverse Laplacian and the parameters $c_{1,2}$. The RSAM being a broadband fast absorber, it is characterized by $J_2 < 0$, $\gamma_2 \gg \gamma_1$, $a \gg 1$ as well as $s \gg 1$.

1) *Injected fields and device coupling:* In the case of a self-imaging configuration, the link between the two devices is achieved by expressing the emitted fields O_j as a combination of the reflection of the injection fields Y_j and the self-emission E_j , which reads

$$O_j(r, t) = \eta_j E_j(r, t) - Y_j(r, t), \quad (5)$$

where we defined $\eta_j = t_1^j / (1 + r_1^j)$ with t_1^j and r_1^j the transmission and reflection coefficients in amplitude of the emitting DBR from the inside to the outside of the cavity. Considering the propagation delay and the losses incurred by the beam-splitter allowing for the light extraction, the link between the two devices is ensured by the following two delayed Algebraic Equations [20]

$$Y_1(r, t) = t_{bs}O_2(r, t - \tau_e), Y_2(r, t) = t_{bs}O_1(r, t - \tau_e), \quad (6)$$

with t_{bs} a complex number whose modulus and phase model the losses induced by the beam-splitter and the single trip feedback phase, respectively.

However, the image of the VCSEL through its collimator is placed exactly at the object focal plane of the collimator in front of the RSAM. In turn, the RSAM is on the image focal plane of its collimator. In this configuration, and assuming that the collimators have a large diameter, the field injected in one device is the (delayed) Fourier transform in space of the field coming from the other, which is modeled via Kirchoff's formula for a lens with focal length f as

$$Y_1(r, t) = t_{bs} \int O_2(r', t - \tau_e) e^{-i\frac{\omega_0}{c} \frac{r \cdot r'}{f}} d^2 r' \equiv \mathcal{F}_\tau(O_2) \quad (7)$$

$$Y_2(r, t) = t_{bs} \int O_1(r', t - \tau_e) e^{-i\frac{\omega_0}{c} \frac{r \cdot r'}{f}} d^2 r' \equiv \mathcal{F}_\tau(O_1) \quad (8)$$

and where the beam-splitter losses may contain a normalization constant due to the Kirchoff's integral. It is worth

remarking that Eqs. (7-8) describe the coupling of the two devices to all orders of reflection in the external cavity. They define a delayed map where the field injected into one device returns inverted. This can be seen, for instance, using Eq. (5) and saying that the RSAM has an effective reflectivity such that $O_j = r_{eff} Y_j$ and substituting in Eq. (7), which yields

$$Y_1(r_\perp, t) = \mu E_1(-r_\perp, t - 2\tau) \quad (9)$$

where we have used that $\mathcal{F}_\tau \circ \mathcal{F}_\tau [Y_2] = \alpha Y_2(-r_\perp, t - 2\tau)$ and $\mu = t_{bs}^2 r_{eff}$ describes the combined effect of the beam splitter and of the RSAM reflection. Thus, after one round-trip, Y_1 overlaps with a spatially reversed copy of itself, and it requires a second round-trip to achieve proper overlap.

2) *Parameters:* The reflectivities of the DBRs in the VCSEL and the RSAM are taken as $(r_1^{(1)}, r_2^{(1)}) = (\sqrt{0.942}, 1)$ and $(r_1^{(2)}, r_2^{(2)}) = (\sqrt{0.59}, 1)$. We assume that the single trip in the VCSEL and the RSAM is $\tau = 30$ fs corresponding to an effective length $L_z = 2.6 \mu\text{m}$ with a index of $n = 3.5$. This gives us $\kappa_1 = 10^{12} \text{ rad.s}^{-1}$ and $\kappa_2 = 10^{13} \text{ rad.s}^{-1}$, yielding a FWHM for the resonances of $\Delta\lambda_j = \kappa_j \lambda_0^2 / (\pi c)$ of 1 nm and 10 nm respectively. Incidentally, we find that $a = 10$ and $(h_1, h_2) = (2, 20)$. The diffraction length is found to

be $L_d = \sqrt{L_z [q_0 (1 - r_1 r_2)]^{-1}} = 2 \mu\text{m}$. We define two numerical domains which are twice the size of the VCSEL and of the RSAM which have both a normalized length $L_\perp = 200$. The other parameters are $\alpha_1 = 2$, $\alpha_2 = 0.5$, $b = 10^{-2}$, $\gamma_1 = 10^{-3}$, $\gamma_2 = 0.1$, $s = 10$, $t_{bs} = 0.9$, $\mathcal{D}_1 = \mathcal{D}_2 = 10^{-3}$, $c_1 = 10^{-2}$ and $c_2 = 10^{-6}$.

3) *Numerical considerations:* The simulation of PML lasers is a very demanding problem from the computational point of view: while pulses may form on a relatively short time scale of a few tens of round-trips, the pulse characteristics only settle on a much longer time scale [21]. If anything, the complex transverse dynamics present in our case shall slow down the dynamics even further. Considering a delay of $\tau_e = 2$ ns and a time step of $\delta t = 10^{-2}$ implies that one must keep four memory buffers for E_j and Y_j of size $(\tau_e \kappa_1 / \delta t) N_x N_y \sim 2 \times 10^3 N_x N_y$ with N_x and N_y the number of mesh points in the two transverse directions. This amounts

to 32 Gigabytes with $N_x = N_y = 512$. Notice in addition that such values of $N_{x,y}$ are not particularly large if one considers that only half of the mesh discretization in the VCSEL is electrically pumped, the rest being used only for letting the field decay to zero and prevent aliasing, a common problem with spectral methods in broad-area lasers, see for instance [22] for a discussion. The time step of $\delta t = 10^{-2}$ is neither particularly small if one considers the stiffness incurred by the RSAM response. For these reasons we restrict our analysis to a single transverse dimension. We believe that the main spatial feature being lost by such simplification is the description of the non mode-locked two dimensional radial flower mode [17] on the border of the VCSEL, which has already been qualitatively discussed. To conclude, for the sake of simplicity, we used a time delay of $\tau_e = 200$ ps (instead of 1 ns) to avoid the temporal complexity of our setup (leading to localized structures, as discussed in [18]), and to concentrate only on the spatial aspects of the problem. We integrated numerically

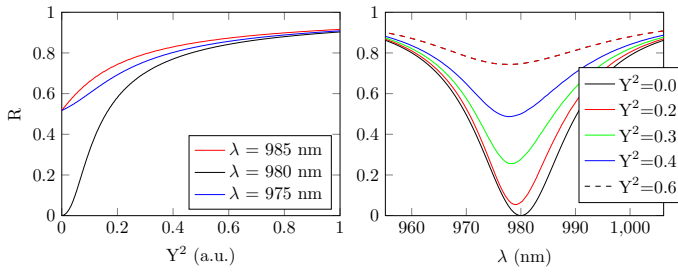


Figure 6. Reflectivity as a function of the input field intensity (left) for various values of the wavelength, the resonance being chosen to be $\lambda_0 = 980$ nm and (right) reflectivity as a function of wavelength for increasing input power.

427 Eqs. (1-4) using a semi-implicit split-step method where
 428 spatial operators are integrated using the Fourier Transform.
 429 Such semi-implicit method is particularly appropriate to the
 430 stiffness induced by the broad response of the RSAM. The
 431 simulation time was 500 single-trips in the external cavity, i.e.
 432 100 ns.

433 4) *RSAM characteristics:* The basic properties of the
 434 RSAM can be found assuming an incoming plane wave of
 435 amplitude Y at normal incidence and at frequency ω i.e.
 436 $Y_2 = Y \exp(-i\omega t)$. The response of the RSAM is given by

$$\left(z - i\omega - \frac{J_2(1 - i\alpha_2)}{1 + s|E_2|^2} \right) E_2 = h_2 Y. \quad (10)$$

437 The effective reflectivities are obtained setting $O_2 = rY_2$
 438 that is to say $r = E_2/Y_2 - 1$ yielding the unsaturated and
 439 saturated responses as

$$r_u = \frac{h_2 - z + i\omega + J_2(1 - i\alpha_2)}{z - i\omega - J_2(1 - i\alpha_2)}, r_s = \frac{h_2 - z + i\omega}{z - i\omega}. \quad (11)$$

440 By choosing $J_2 = a - h_2$ we obtain a perfectly absorbing
 441 RSAM, i.e. $r_u = 0$ at the frequency $\omega = \delta + \alpha(a - h_2)$. In
 442 between these unsaturated and saturated regimes, the effective
 443 reflectivity can be obtained by solving Eq. (10) numerically.
 444 We represent the results of this procedure for $R = |r|^2$ in
 445 Fig. 6.

446 5) *Defect in the RSAM surface:* We assume that the impu-
 447 rity on the RSAM surface has the effect of locally lowering
 448 the reflectivity of the top mirror. As such the parameters a and
 449 h_2 are allowed to vary in the transverse dimension. A decrease
 450 of $r_1^{(2)}$ of 0.1 modifies a and h_2 to be $a = 12$ and $h_2 = 24$.
 451 We assume a Gaussian profile for such transverse variations
 452 whose FWHM is $\sim 4.7 \mu\text{m}$.

453 A. Mode-Locking dynamics

454 The bias current is fixed to $J_1 = 0.92$, i.e. below the
 455 threshold of the solitary VCSEL but above the threshold of the
 456 compound device. We depict in Fig. 7, the output time trace
 457 for the intensity averaged over the surface of the VCSEL as
 458 well as the averaged population inversion in the active region
 459 of the VCSEL and in the RSAM. One recognizes the standard
 460 PML temporal pattern where the gain experiences depletion
 461 during the passing of the pulse followed by an exponential
 462 recovery. The same yet inverted pattern is also visible on the
 463 RSAM population inversion. We found the pulse width to be

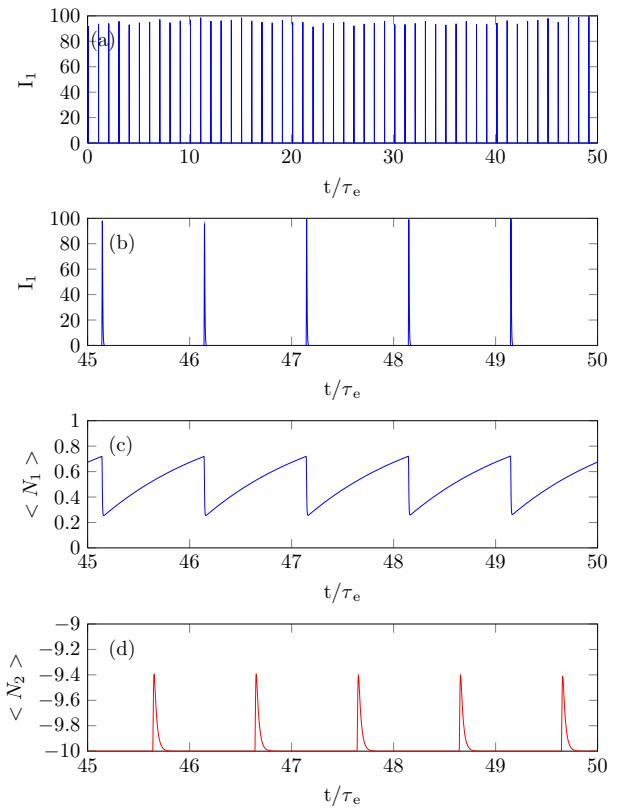


Figure 7. Panels a) and b): Averaged Intensity profile I_1 as a function of time showing stable PML. Panels c) and d) represent the averaged population inversion in the VCSEL and in the RSAM as a function of time.

464 of the order of 4 ps, in good qualitative agreement with the
 465 experimental results.

466 Such averaged representation describes well the experimen-
 467 tal situation when the full output of the VCSEL is captured by
 468 the photo-detector. Yet it does not shed light onto the hidden
 469 transverse dynamics. We represent in Fig. 8 the spatially
 470 resolved temporal output of the VCSEL. In Fig. 8a) the phase
 471 profile $\phi_1 = \arg(E_1)$ discloses the existence of alternate
 472 transverse waves while the intensity profile in Fig. 8b) remains
 473 uniform. Such field profile directly impings the RSAM via its
 474 Fourier Transform which explains that the temporal time trace
 475 of population inversion in the RSAM (Fig. 8c)) exhibits two
 476 spots at two opposite locations with respect to its center. In
 477 Fig. 8c) we represented the center of the pinning potential with
 478 a dotted line while the two white lines represent its FWHM.
 479 The horizontal axis in Fig. 8c) is scaled in normalized spatial
 480 frequencies. The transverse value of the wave vector here is
 481 ~ 16 which corresponds to 8 transverse oscillations along the
 482 active region of the VCSEL, i.e. a wavelength of $\sim 25 \mu\text{m}$.

483 We found that by slowly displacing the center of the pinning
 484 potential it was possible to tune the normalized transverse
 485 wave vector between $q_x L = 0$ and $q_x L = 36$, which
 486 corresponds to a minimal wavelength of $11 \mu\text{m}$. The associated
 487 shift in the emission wavelength is ~ 4 nm around 980 nm,
 488 in excellent agreement with the experimental results. Several
 489 points along such tuning curve are presented in Fig. 9. All
 490 cases correspond to stable PML regimes that would seem to

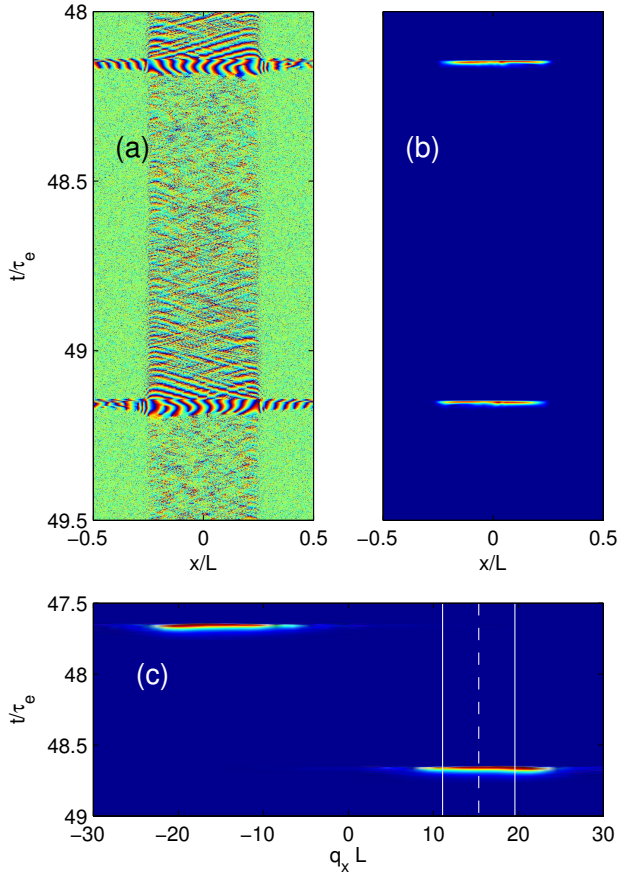


Figure 8. Panel a): Phase profile of E_1 as a function of space and time. A tilted wave with alternate wave vector from one round-trip to the next is clearly visible. Panel b) Intensity profile of E_1 showing that the transverse intensity profile is uniform. Panel c): Population inversion in the RSAM. The FWHM size of the population inversion spot is $\sim 6 \mu\text{m}$ and the RSAM is fully saturated locally by the pulse.

be almost identical if one would consider only the averaged temporal output like e.g. in Fig. 7. Noteworthy, we also found some perfectly regular PML regimes when the inhomogeneity was located at the center of the RSAM. We provide several explanations for such discrepancy. First, the dissipation of the energy and of the associated heat incurred by the light absorption is doubled when the two spots are well separated onto the RSAM. Such thermal effects are not taken in consideration by our model. Second, other spatial inhomogeneities, these ones detrimental to PML, could very well be located on the sides of the pinning defect favoring PML. When the two spots become less and less separated experimentally, the spot that is not experiencing the pinning defect (i.e. the left spot in Fig. 9) will eventually be the victim of such other detrimental inhomogeneities.

V. CONCLUSIONS

We have shown that electrically biased broad-area VCSELs with optical feedback from a RSAM can be passively mode-locked when the VCSEL and RSAM are placed each at the Fourier plane of the other. In this configuration, the system emits a train of pulses of ~ 10 ps width with a period equal

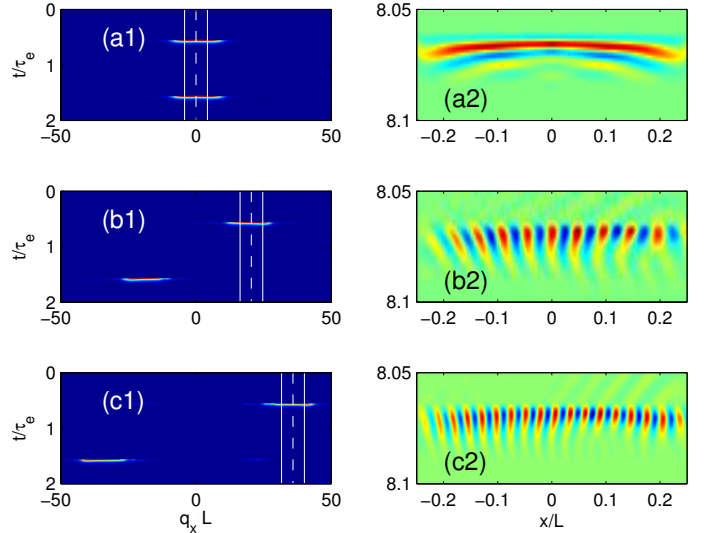


Figure 9. Evolution of the transverse wave vector as a function of the position of the pinning potential. Panels a1), b1) and c1) correspond to the population inversion in the RSAM while the panels a2), b2) and c2) correspond to the real part of E_1 . The FWHM size of the population inversion spot in the RSAM corresponds to $\sim 6 \mu\text{m}$ and the RSAM is fully saturated locally by the pulse.

to the round-trip time of the external cavity τ_e . In this PML regime the time-averaged VCSEL far-field, which is imaged onto RSAM plane, exhibits two bright peaks symmetrically located around the optical axis, thus indicating that the VCSEL emits two tilted waves with opposite transverse components. The time traces corresponding to each spot consist of a pulse train with a period $2\tau_e$, and the two trains are delayed by one round-trip one with respect to the other. Accordingly, the two tilted waves are alternatively emitted at every round-trip. We have shown that the mechanism leading to wave vector selection is related to the existence of inhomogeneities in the transverse section of the RSAM. Because the RSAM is in the Fourier plane of the VCSEL near-field, a defect may favor a tilted wave emission with a well-defined transverse component. By shifting the RSAM laterally, the defect moves in the Fourier plane, thus selecting another transverse wave vector and allowing for wavelength tuning of the mode-locked emission.

VI. APPENDIX

Our approach extends the methodology developed in [23] for single-mode VCSELs under optical injection to the case of broad-area devices. The Quantum-Well active region is considered as infinitely thin, and the wave equation is exactly solved inside the cavity for monochromatic plane-waves. Transforming back to a spatio-temporal representation provides the time-domain evolution of the field inside cavity. Finally, the coupling of the two cavities is included by describing how the injection terms depend on the intra-cavity fields.

The starting point is the scalar Maxwell equation for a monochromatic field as in [23]

$$(\partial_z^2 + \Delta_\perp) \mathcal{E}(\omega, \vec{r}) + \frac{\omega^2}{v^2} \mathcal{E}(\omega, \vec{r}) = \frac{-\omega^2}{c^2 \epsilon_0} \mathcal{P}(\omega, \vec{r}), \quad (12)$$

542 where $\Delta_{\perp} = \partial_x^2 + \partial_y^2$, \mathcal{P} is the polarization of the QW 574 $\partial_{\omega} F_1$ is purely imaginary, and the field evolution can be
 543 active region and $v = c/n$ with n the index of refraction. In 575 written as
 544 the longitudinal direction, the cavity is defined by two Bragg
 545 mirrors at $z = 0$ and $z = L$.

546 Fourier transforming over the transverse coordinates yields

$$\left(\partial_z^2 + \frac{\omega^2}{v^2} - q_{\perp}^2 \right) \mathcal{E}(\omega, q_{\perp}, z) = \frac{-\omega^2 W}{c^2 \varepsilon_0} P(\omega, q_{\perp}) \delta_l. \quad (13)$$

547 We assumed that the Quantum Well(s) of width $W \ll \lambda$ are 578 at resonance, $L_{diff} \approx |r_1 r_2| \frac{2v \partial_{q_{\perp}^2} L_e}{\omega_0}$ is the diffraction length,
 548 located at $z = l$ and defined $\delta_l = \delta(z - l)$. In the empty 579 and C describes the variation of cavity losses with the angle
 549 regions where there is no polarization the solution of Eq. (13) 580 of incidence.

550 reads

$$\mathcal{E}(\omega, q_{\perp}, z) = \begin{cases} L_+ e^{iQz} + L_- e^{-iQz} & \text{if } 0 < z < l \\ R_+ e^{iQz} + R_- e^{-iQz} & \text{if } l < z < L \end{cases} \quad (14)$$

551 where the longitudinal wave vector $Q(q_{\perp}, \omega) = \sqrt{\frac{\omega^2}{v^2} - q_{\perp}^2}$. 584 where α is Henry's linewidth enhancement factor, g_0 is the
 552 The boundary conditions at the mirrors and at the QW impose 585 material gain coefficient and N_t is the transparency carrier
 553 that 586 density. The carrier density, in turn, obeys the standard de-

$$r_1 L_- + t'_1 Y = L_+ \quad (15)$$

$$r_2 R_+ e^{iQL} = R_- e^{-iQL} \quad (16)$$

$$L(l) = R(l) = \mathcal{E}(\omega, q_{\perp}, l) \quad (17)$$

$$\partial_z R(l) - \partial_z L(l) = -\frac{\omega^2}{\varepsilon_0 c^2} P \quad (18)$$

554 where the primed indexes are for transmission and reflection 589 where γ is the scaled carrier lifetime, J is the current injection
 555 processes starting outside of the cavity, r_1 and r_2 the top 590 above transparency, \mathcal{D} is the diffusion coefficient and h
 556 (emitting) and bottom reflectivities and Y is the amplitude of 591 describes the coupling of the output field onto the QW and
 557 the external field impinging on the device. After some algebra 592 reads
 558 the equation linking \mathcal{E} , P and Y is found to be

$$h = t'_1 \frac{1 + r_2}{1 - r_1 r_2} \quad (26)$$

$$F_1(Q) \mathcal{E} = -\frac{\omega^2}{2iQ\varepsilon_0 c^2} \Gamma W P + F_2(Q) Y \quad (19)$$

559 with

$$F_1 = (1 - r_1 r_2 e^{2iQL}), F_2 = t'_1 e^{iQL} (1 + r_2 e^{2iQ(L-l)}). \quad (20)$$

560 The modes of the VCSEL correspond to the minima of
 561 F_1 , and the QW is placed in order to maximize the optical
 562 confinement factor $\Gamma = (1 + r_1 e^{2iQL}) (1 + r_2 e^{2iQ(L-l)})$ for
 563 the fundamental mode at $q_{\perp} = 0$. For fixed magnitude of the
 564 reflectivities, this is achieved by imposing that

$$2\frac{\omega}{v}l + \phi_1 = 2\pi n_1, 2\frac{\omega}{v}(L-l) + \phi_2 = 2\pi n_2$$

565 where $\phi_{1,2}$ are the phases of the reflectivities $r_{1,2}$ and n_1 and
 566 n_2 two integers. Thus the modal frequencies are determined by
 567 the effective cavity length $L_e = L + 2v(\phi_1 + \phi_2)/\omega$. Around 604
 568 any modal frequency ω_0 , and in paraxial conditions, F_2 and
 569 Γ/Q vary much more slowly than F_1 . In order to have a spatio-
 570 temporal description of the dynamics of the field, we then fix
 571 Γ/Q and F_2 and expand

$$F_1 = F_1^0 + (\omega - \omega_0) \partial_{\omega} F_1 + q_{\perp}^2 \partial_{q_{\perp}^2} F_1 + \dots \quad (21)$$

572 and transform back to space and time using that $\omega \rightarrow \omega_0 + i\partial_t$ 610 38864-C03-01) and from the Direcció General de Recerca,
 573 and $q_{\perp}^2 \rightarrow -\Delta_{\perp}$. Since F_1 is at a minimum of its modulus, 611 Desenvolupament Tecnològic i Innovació de la Conselleria

$$\tau_c \frac{d\mathcal{E}}{dt} = i \frac{\omega_0 \Gamma W}{2n\varepsilon_0 c} P - \kappa \tau_c \mathcal{E} + i L_{diff}^2 \Delta_{\perp} \mathcal{E} + t'_1 (1 + |r_2|) (-1)^m Y + C \Delta_{\perp}^2 \mathcal{E} \quad (22)$$

577 $\kappa \approx 1 - |r_1 r_2|$ are the cavity losses under normal incidence

578 at resonance, $L_{diff} \approx |r_1 r_2| \frac{2v \partial_{q_{\perp}^2} L_e}{\omega_0}$ is the diffraction length,
 579 and C describes the variation of cavity losses with the angle
 580 of incidence.

581 The polarization of the QW active region determines the
 582 gain and index change induced by the carriers, and we adopt
 583 the simple adiabatic approximation

$$P = \varepsilon_0 (\alpha - i) g_0 (N - N_t) E \quad (23)$$

584 where α is Henry's linewidth enhancement factor, g_0 is the
 585 material gain coefficient and N_t is the transparency carrier
 586 density. The carrier density, in turn, obeys the standard de-
 587 scription as in [23]. Upon normalization, the evolution for the
 588 field and carrier density can be written as

$$\frac{\partial E}{\partial t} = [(1 - i\alpha)N - 1 + i\Delta_{\perp} + c\Delta_{\perp}^2] E + hY, \quad (24)$$

$$\frac{\partial N}{\partial t} = \gamma [J - (1 + |E|^2)N] + \mathcal{D}\Delta_{\perp} N, \quad (25)$$

589 where γ is the scaled carrier lifetime, J is the current injection
 590 above transparency, \mathcal{D} is the diffusion coefficient and h
 591 describes the coupling of the output field onto the QW and
 592 reads

$$h = t'_1 \frac{1 + r_2}{1 - r_1 r_2}$$

593 As a last step, we evaluate the field at the laser output O as
 594 a combination of the reflection of the injected beam $r'_1 Y$ as
 595 well as transmission of the left intra-cavity propagating field
 596 L_- , i.e. $O = t_1 L_- + r'_1 Y$. Around resonance and using the
 597 Stokes relations $tt' - rr' = 1$ and $r' = -r$ we find, defining
 598 $\eta = t_1 / (1 + r_1)$

$$O = \eta (-1)^m \mathcal{E} - Y \quad (27)$$

599 although the $(-1)^m$ is irrelevant in the sense that the QW
 600 experiences also a field with a $(-1)^m$ which can therefore
 601 be removed. In the case of two devices, we scale the photon
 602 lifetime, the coupling and the saturation field with respect to
 603 the first one leading to the following definitions

$$h_2 = t'_3 \frac{1 + r_4}{1 - r_1 r_2} \frac{r_1 r_2}{r_3 r_4}, a = \frac{1 - r_3 r_4}{1 - r_1 r_2} \frac{r_1 r_2}{r_3 r_4}, b = \frac{r_1 r_2}{r_3 r_4} \quad (28)$$

$$\text{and } s = (g_2 \gamma_1) / (g_1 \gamma_2).$$

ACKNOWLEDGMENT

606 J.J. acknowledges financial support from the Ramon y Cajal
 607 fellowship and the CNRS for supporting a visit at the INLN
 608 where part of his work was developed. J.J. and S.B. acknowl-
 609 edge financial support from project RANGER (TEC2012-

d'Innovació, Interior i Justícia del Govern de les Illes Balears co-funded by the European Union FEDER funds. M.M. and M.G. acknowledge funding of Région PACA with the Projet Volet Général 2011 GEDEPULSE.

REFERENCES

- [1] A. Gordon and B. Fischer, "Phase transition theory of many-mode ordering and pulse formation in lasers," *Physical Review Letters*, vol. 89, pp. 103 901–3, 2002.
- [2] H. A. Haus, "Mode-locking of lasers," *IEEE J. Selected Topics Quantum Electron.*, vol. 6, pp. 1173–1185, 2000.
- [3] —, "Theory of mode locking with a fast saturable absorber," *Journal of Applied Physics*, vol. 46, pp. 3049–3058, 1975.
- [4] —, "Theory of mode locking with a slow saturable absorber," *Quantum Electronics, IEEE Journal of*, vol. 11, pp. 736–746, 1975.
- [5] H. Dorren, D. Lenstra, Y. Liu, M. Hill, and G.-D. Khoe, "Nonlinear polarization rotation in semiconductor optical amplifiers: theory and application to all-optical flip-flop memories," *Quantum Electronics, IEEE Journal of*, vol. 39, no. 1, pp. 141–148, Jan 2003.
- [6] E. P. Ippen, "Principles of passive mode locking," *Appl. Phys. B*, vol. 58, pp. 159–170, 1994.
- [7] J. Javaloyes, J. Mulet, and S. Balle, "Passive mode locking of lasers by crossed-polarization gain modulation," *Phys. Rev. Lett.*, vol. 97, p. 163902, Oct 2006. [Online]. Available:
- [8] K. G. Wilcox, Z. Mihoubi, G. J. Daniell, S. Elsmere, A. Quarterman, I. Farrer, D. A. Ritchie, and A. Tropper, "Ultrafast optical stark mode-locked semiconductor laser," *Opt. Lett.*, vol. 33, no. 23, pp. 2797–2799, 2008.
- [9] R. Fork, C. Shank, R. Yen, and C. Hirlimann, "Femtosecond optical pulses," *Quantum Electronics, IEEE Journal of*, vol. 19, no. 4, pp. 500–506, apr 1983.
- [10] U. Keller, K. J. Weingarten, F. X. Kärtner, D. Kopf, B. Braun, I. D. Jung, R. Fluck, C. Hönninger, N. Matuschek, and J. Aus der Au, "Semiconductor saturable absorber mirrors (SESAM's) for femtosecond to nanosecond pulse generation in solid-state lasers," *Selected Topics in Quantum Electronics, IEEE Journal of*, vol. 2, pp. 435–453, 1996.
- [11] E. A. Avrutin, J. H. Marsh, and E. L. Portnoi, "Monolithic and multi-GigaHertz mode-locked semiconductor lasers: Constructions, experiments, models and applications," *IEE Proc.-Optoelectron.*, vol. 147, pp. 251–278, 2000.
- [12] B. Rudin, V. J. Wittwer, D. J. H. C. Maas, M. Hoffmann, O. D. Sieber, Y. Barbarin, M. Golling, T. Südmeyer, and U. Keller, "High-power mixsel: an integrated ultrafast semiconductor laser with 6.4 w average power," *Opt. Express*, vol. 18, no. 26, pp. 27 582–27 588, Dec 2010. [Online]. Available:
- [13] K. G. Wilcox, A. C. Tropper, H. E. Beere, D. A. Ritchie, B. Kunert, B. Heinen, and W. Stolz, "4.35 kw peak power femtosecond pulse mode-locked vcsel for supercontinuum generation," *Opt. Express*, vol. 21, no. 2, pp. 1599–1605, Jan 2013. [Online]. Available:
- [14] I. Fischer, O. Hess, W. Elsässer, and E. Göbel, "Complex spatio-temporal dynamics in the near-field of a broad-area semiconductor laser," *Europhys. Lett.*, vol. 35, pp. 579–584, 1996.
- [15] G. H. B. Thompson, "A theory for filamentation in semiconductor lasers including the dependence of dielectric constant on injected carrier density," *Opto-electronics*, vol. 4, pp. 257–310, 1972.
- [16] M. Grabherr, R. Jager, M. Miller, C. Thalmaier, J. Herlein, R. Michalzik, and K. Ebeling, "Bottom-emitting vcsel's for high-cw optical output power," *Photonics Technology Letters, IEEE*, vol. 10, no. 8, pp. 1061–1063, Aug 1998.
- [17] I. V. Babushkin, N. A. Loiko, and T. Ackemann, "Eigenmodes and symmetry selection mechanisms in circular large-aperture vertical-cavity surface-emitting lasers," *Phys. Rev. E*, vol. 69, p. 066205, Jun 2004. [Online]. Available:
- [18] M. Marconi, J. Javaloyes, S. Balle, and M. Giudici, "How lasing localized structures evolve out of passive mode locking," *Phys. Rev. Lett.*, vol. 112, p. 223901, Jun 2014. [Online]. Available:
- [19] J. Oudar, R. Kuszelewicz, B. Sfez, J. Michel, and R. Planel, "Prospects for further threshold reduction in bistable microresonators," *Optical and Quantum Electronics*, vol. 24, no. 2, pp. S193–S207, 1992. [Online]. Available:
- [20] J. Javaloyes and S. Balle, "Multimode dynamics in bidirectional laser cavities by folding space into time delay," *Opt. Express*, vol. 20, no. 8, pp. 8496–8502, Apr 2012. [Online]. Available:
- [21] —, "Mode-locking in semiconductor Fabry-Pérot lasers," *Quantum Electronics, IEEE Journal of*, vol. 46, no. 7, pp. 1023–1030, July 2010.
- [22] A. Perez-Serrano, J. Javaloyes, and S. Balle, "Spectral delay algebraic equation approach to broad area laser diodes," *Selected Topics in Quantum Electronics, IEEE Journal of*, vol. PP, no. 99, pp. 1–1, 2013.
- [23] J. Mulet and S. Balle, "Mode locking dynamics in electrically-driven vertical-external-cavity surface-emitting lasers," *Quantum Electronics, IEEE Journal of*, vol. 41, no. 9, pp. 1148–1156, 2005.



Mathias Marconi was born in Nice, France, in 1988. From 2006 to 2011, he was a student at Université de Nice Sophia Antipolis (UNS), France. In 2011, he was an exchange student at Strathclyde university, Glasgow, U.K. The same year he obtained the Master degree in optics from UNS. He is currently pursuing the Ph.D. degree at the Institut Non-linéaire de Nice, Valbonne, France. His research interests include semiconductor laser dynamics and pattern formation in out of equilibrium systems. He is a member of the European Physical Society.



Julien Javaloyes (M'11) was born in Antibes, France in 1977. He obtained his M.Sc. in Physics at the ENS Lyon the PhD in Physics at the Institut Non Linéaire de Nice / Université de Nice Sophia-Antipolis working on recoil induced instabilities and self-organization processes in cold atoms. He worked on delay induced dynamics in coupled semiconductor lasers, VCSEL polarization dynamics and monolithic mode-locked semiconductor lasers. He joined in 2010 the Physics Department of the Universitat de les Illes Balears as a Ramón y Cajal fellow. His research interests include laser dynamics and bifurcation analysis.



Salvador Balle (M'92) was born in Manacor, Mallorca. He graduated in Physics at the Universitat Autònoma de Barcelona, where he obtained a PhD in Physics on the electronic structure of strongly correlated Fermi liquids. After postdoctoral stages in Palma de Mallorca and Philadelphia where he became interested in stochastic processes and Laser dynamics, he joined in 1994 the Physics Department of the Universitat de les Illes Balears, where he is Professor of Optics since 2006. His research interests include laser dynamics, semiconductor optical response modeling, multiple phase fluid dynamics and laser ablation.



Massimo Giudici (M'09) received the "Laurea in Fisica" from University of Milan in 1995 and Ph.D from Université de Nice Sophia-Antipolis in 1999. He is now full professor at Université de Nice Sophia-Antipolis and deputy director of the laboratory "Institut Non Linéaire de Nice", where he carries out his research activity. Prof. Giudici's research interests revolve around the spatio-temporal dynamics of semiconductor lasers. In particular, he is actively working in the field of dissipative solitons in these lasers. His most important contributions concerned Cavity Solitons in VCSELs, longitudinal modes dynamics, excitability and stochastic resonances in semiconductor lasers and the analysis of lasers with optical feedback. He is authors of more than 50 papers and he is Associated Editor of IEEE Photonics Journal.